JGR Atmospheres

RESEARCH ARTICLE
10.1029/2018JD029860

Special Section:
Atmospheric Rivers: Intersection of Weather and Climate

Key Points:
- All U.S. West Coast subregions exhibit positive atmospheric river (AR) temperature trends, with warming ranging from 0.69 to 1.65 °C over the study period
- AR warming magnitude exhibits seasonal and regional asymmetry; ARs have warmed by more than 2 °C in some months, particularly in March
- AR warming at landfall is influenced by temperature trends over the coastal ocean, over the landfall region, and along the AR tracks

Supporting Information:
- Supporting Information S1

Correspondence to:
K. R. Gonzales,
kgonzal@stanford.edu

Citation:
Gonzales, K. R., Swain, D. L., Nardi, K. M., Barnes, E. A., & Diffenbaugh, N. S. (2019). Recent warming of landfalling atmospheric rivers along the west coast of the United States. *Journal of Geophysical Research: Atmospheres*, *124*. https://doi.org/10.1029/2018JD029860

Received 23 OCT 2018
Accepted 10 MAY 2019
Accepted article online 30 MAY 2019

Recent Warming of Landfalling Atmospheric Rivers Along the West Coast of the United States

Katerina R. Gonzales[1], **Daniel L. Swain**[2,3,4], **Kyle M. Nardi**[5], **Elizabeth A. Barnes**[5], **and Noah S. Diffenbaugh**[1,6]

[1]Department of Earth System Science, Stanford University, Stanford, CA, USA, [2]Institute of the Environment and Sustainability, University of California, Los Angeles, CA, USA, [3]Capacity Center for Climate and Weather Extremes, National Center for Atmospheric Research, Boulder, CO, USA, [4]The Nature Conservancy of California, San Francisco, CA, USA, [5]Department of Atmospheric Science, Colorado State University, Fort Collins, CO, USA, [6]Woods Institute for the Environment, Stanford University, Stanford, CA, USA

Abstract Atmospheric rivers (ARs) often generate extreme precipitation, with AR temperature strongly influencing hydrologic impacts by altering the timing and magnitude of runoff. Long-term changes in AR temperatures therefore have important implications for regional hydroclimate—especially in locations where a shift to more rain-dominated AR precipitation could affect flood risk and/or water storage in snowpack. In this study, we provide the first climatology of AR temperature across five U.S. West Coast subregions. We then assess trends in landfalling AR temperatures for each subregion from 1980 to 2016 using three reanalysis products. We find AR warming at seasonal and monthly scales. Cool-season warming ranges from 0.69 to 1.65 °C over the study period. We detect monthly scale warming of >2 °C, with the most widespread warming occurring in November and March. To understand the causes of AR warming, we quantify the density of AR tracks from genesis to landfall and analyze along-track AR temperature for each month and landfall region. We investigate three possible influences on AR temperature trends at landfall: along-track temperatures prior to landfall, background temperatures over the landfall region, and AR temperature over the coastal ocean adjacent to the region of landfall. Generally, AR temperatures at landfall more closely match coastal and background temperature trends than along-track AR temperature trends. The seasonal asymmetry of the AR warming and the heterogeneity of influences have important implications for regional water storage and flood risk—demonstrating that changes in AR characteristics are complex and may not be directly inferred from changes in the background climate.

Plain Language Summary Atmospheric river (AR) storms are well known for their ability to accumulate snowpack, provide drought relief, and generate extreme precipitation and flooding along the West Coast of the United States. AR temperature is an important variable for determining the water resource impacts of a given event, such as the ratio of rain to snow delivered by an individual storm. As a result, changes in AR temperature have implications for both water storage and flood risk. We find substantial warming in ARs at both the seasonal and monthly scales, as well as seasonal and regional variations in the amount of warming along the U.S. West Coast. To understand the warming of ARs at the landfall regions, we compare these trends with trends in temperature along the AR tracks, background temperature over the landfall region, and temperature over the coastal ocean adjacent to the landfall region. The most robust warming occurs in November and March, which has important implications for increased regional flood risk and decreased water storage, and motivates further investigation in other AR-prone regions around the globe.

1. Introduction

Atmospheric rivers (ARs) are long, narrow, filamentary plumes of moisture that are responsible for ~90% of poleward moisture transport (Zhu & Newell, 1998). ARs are characterized by strong moisture transport, which is most concentrated in the lower levels of the atmosphere (Ralph et al., 2005). Although ARs occur globally (Waliser & Guan, 2017), they are of particular interest in regions in which ARs induce extreme precipitation and/or bring a substantial fraction of overall precipitation.

The U.S. West Coast meets both of these criteria: ARs deliver 30–50% of California's precipitation (Dettinger, 2011), are crucial for snowpack (Guan et al., 2010), and also induce hazards such as extreme precipitation, wind, floods, and mudslides (Neiman et al., 2011; Oakley et al., 2018; Ralph et al., 2006; Waliser & Guan, 2017). The simultaneous dependence on and vulnerability to ARs along the West Coast has motivated substantial research into the sensitivity of AR characteristics to global and regional climate variability and change (e.g., Dettinger, 2011; Gao et al., 2015; Gershunov et al., 2017; Hagos et al., 2016; Payne & Magnusdottir, 2015; Ramos et al., 2016; Shields & Kiehl, 2016a; Warner et al., 2015).

The western U.S. is already experiencing the consequences of regional warming, including increased risk of drought (Diffenbaugh et al., 2015), increased frequency of both wet and dry extremes (Swain et al., 2016), and earlier timing of snowmelt (Cayan et al., 2001). In the Sierra Nevada, the elevation of the mean snow line has risen sharply over the past 15 years (Hatchett et al., 2017), resulting in an increased fraction of high elevation precipitation falling as rain rather than snow. Higher snow levels and increasing rain fraction are expected to yield higher magnitude floods in this region (Das et al., 2011). The extremely wet year of 2016–2017 provides a clear example of this regime, as increased temperatures produced substantially higher runoff due to precipitation falling as rain rather than snow (Huang et al., 2018). Likewise, the western U.S. has experienced a snowpack loss of 21% in the past century due to regional warming (Mote et al., 2018), associated with decreased snow accumulation and increased snowmelt (Kapnick & Hall, 2012).

These historical changes motivate the need to better understand how global warming could impact the AR characteristics that shape water supply and hydroclimatic risk. A number of changes to AR characteristics have been observed and/or hypothesized in recent years, including observed increases in integrated water vapor transport (IVT) in North Pacific ARs (Gershunov et al., 2017), projected increases in AR length and width (Espinoza et al., 2018), projected changes to the frequency of AR events and/or AR conditions (e.g., Espinoza et al., 2018; Gao et al., 2015; Shields & Kiehl, 2016a), and projected increases in the frequency of extreme precipitation associated with ARs (Hagos et al., 2016; Shields & Kiehl, 2016b).

It has also been projected that air temperatures during AR events could warm considerably in response to elevated greenhouse forcing (e.g., Dettinger, 2011; Guan et al., 2010). For example, late-century December–February (DJF) surface air temperatures during California ARs are projected to increase by ~2 °C (Dettinger, 2011). However, AR temperature has not been evaluated beyond the surface air temperature during AR days, meaning that the temperature of three-dimensional AR objects has not yet been characterized. Furthermore, despite projections of future AR warming, historical trends in AR temperature have not yet been assessed.

Increases in AR temperature would have important implications for current and future water availability and flood risk. Cool-season precipitation has been warming across much of the western U.S. in recent decades, leading to decreases in the proportion of precipitation falling as snow (Knowles et al., 2006). However, because ARs generate roughly four times as much snow water equivalent as non-AR storms (Guan et al., 2010), distinguishing trends in AR temperature will be critical for understanding shifting snow-to-rain ratios and the probability of rain-on-snow hazards in mountainous regions.

The impacts of AR temperature trends are particularly relevant in the western U.S. First, within the western U.S., a very small number of individual AR storms contribute disproportionately to water supply or flood hazards in a particular basin. Second, surface air temperatures during AR events exert considerable influence on snow accumulation totals (Guan et al., 2010), with warm air temperatures associated with higher snowlines (Dettinger, 2011). Third, elevated AR temperatures are especially characteristic of exceptionally warm and moist Pineapple Express-type ARs, the tropical origins of which tend to increase the potential for adverse hydrological impacts in regions with substantial winter snowpack (Guan et al., 2016; Hatchett et al., 2018). Long-term warming of ARs could thus increase the snowline elevation, decrease snow accumulation, and decrease the probability that an individual AR will bring snow.

Because of the remote tropical moisture source of some ARs, future changes in landfalling AR temperature are projected to occur at different rates than those of overall cool-season precipitation (Dettinger, 2011). Because ARs may contain advected moisture from remote source regions (Bao et al., 2006; Ralph et al., 2011) and/or local recycled moisture (Dacre et al., 2015; Sodemann & Stohl, 2013), both remote and local temperature trends may be relevant. Furthermore, if the trajectories of ARs across the Pacific differ by landfall region and/or time of year, that spatial and seasonal complexity could also influence AR temperature trends. Thus, the relative influence of temperature trends at and adjacent to the landfall region versus temperature trends along the AR track will be a key question for understanding trends in landfalling AR temperatures along the U.S. West Coast.

2. Materials and Methods

2.1. Overview of Methods

Our goal is to measure AR temperature trends using a metric that (1) captures the temperature of the most relevant portion of the AR, both in its horizontal and vertical dimensions, and (2) can be employed flexibly and robustly across different AR catalogs and reanalysis products.

Many AR catalogs have been developed using varying AR definitions, AR detection algorithms, and reanalysis data sets (Shields et al., 2018). We use an AR catalog (described in section 2.3.) to identify ARs that cross U.S. West Coast grid boxes (Figure S1 in the supporting information). The catalog records the date, time, and other metrics (e.g., length and orientation) for the detected AR object. We then retrieve associated moisture, wind, and temperature fields from the ERA-Interim, MERRA-2, and NCEP-DOE reanalyses (Dee, 2011; Gelaro et al., 2017; Kanamitsu et al., 2002; respectively; section 2.2) for all dates on the AR catalog.

We define five contiguous study regions along the West Coast, from the U.S./Canada border in Washington to the U.S./Mexico border in California (Figure 1a inset). The regions are chosen to span similar meridional extents and to contain similar land-to-ocean ratios. We next characterize the temperature of each AR (section 2.4) across three satellite-era reanalyses, producing a daily scale time series of AR landfall temperatures for each region. We conduct this characterization separately for each reanalysis product and then average the daily temperature values of each time series to produce a single multireanalysis ensemble mean AR temperature time series for each region. From these time series, we assess trends in AR landfall temperatures at the seasonal and monthly scales (section 2.5). Finally, we investigate the source of landfalling AR temperature trends by comparing them with trends in background temperature at the landfall destination region, trends in AR track temperature (section 2.6), and trends in prelandfall coastal AR temperature (to test the influence of coastal sea surface temperatures, SSTs). To calculate along-track temperatures, we first track the landfalling ARs' back trajectories from the destination region to the genesis region (section 2.6.2), which yields track density plots for each month and region of eventual landfall.

2.2. Data

Atmospheric reanalysis products provide the capability to continuously measure ARs across the globe during the satellite era. Horizontal resolution plays a role in AR detection (Jackson et al., 2016; Shields et al., 2018), as algorithms may fail to detect ARs in low resolution products (Jackson et al., 2016). However, products with coarser spatial resolution have successfully been employed in AR studies (Guan & Waliser, 2015; Ralph et al., 2018). Subdaily time resolution is also important because ARs are transient and highly filamentary, with an average landfalling time of only 20 hr (Ralph et al., 2013).

The ERA-Interim (ERA-I; Dee, 2011), Modern-Era Retrospective Analysis for Research and Applications (MERRA; Rienecker et al., 2011), and NCEP Climate System Forecast Reanalysis (CSFR; Saha et al., 2010) products have been documented in capturing AR characteristics found in satellite observations (Jackson et al., 2016), with ERA-I exhibiting the smallest bias in AR frequency and landfall latitude. In order to evaluate the robustness of our results across multiple reanalysis data sets, we conduct our analysis on MERRA-2 (the product on which the AR detection algorithm in Mundhenk et al., 2016,–hereafter MBM16–is run and the preferred product in the AR Tracking Method Intercomparison Project; Shields et al., 2018), along with ERA-I (a product used in numerous AR studies; e.g., Guan & Waliser, 2015), and NCEP-DOE R2 (a lower resolution product that also spans the satellite era). The horizontal resolution varies by product: ~$0.5° \times 0.5°$ for MERRA-2, ~$0.75° \times 0.75°$ for ERA-I, and $2.5° \times 2.5°$ for NCEP-DOE.

2.3. AR Catalog

We employ a U.S. West Coast AR catalog using a detection algorithm based on MBM16. The catalog detects ARs over the North Pacific basin from 1980 to 2016, using MERRA-2 reanalysis (Gelaro et al., 2017). The catalog's algorithm uses anomalous IVT for AR detection and employs a Lagrangian approach to detect AR objects over a large domain across consecutive time slices.

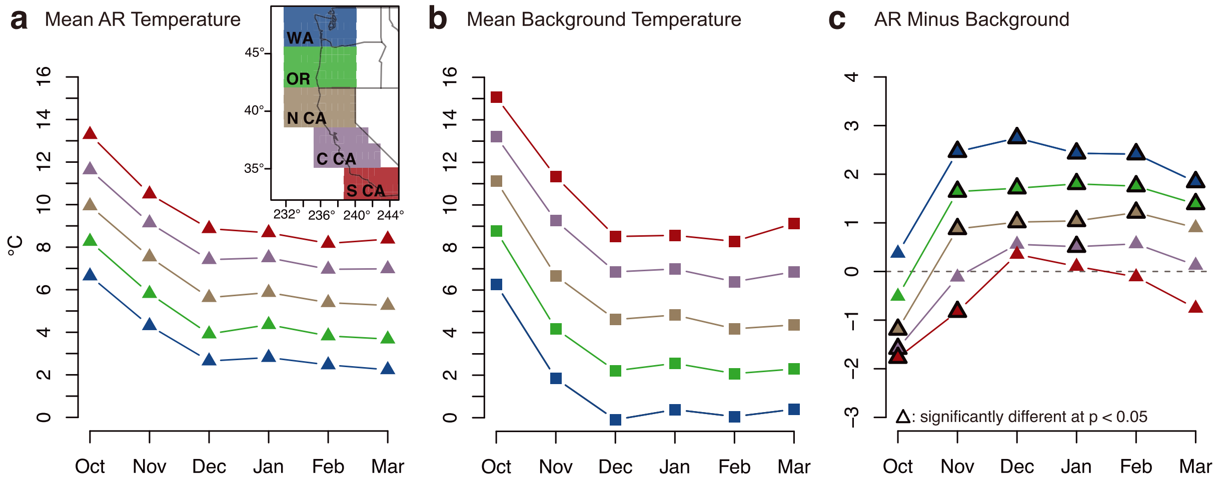

Figure 1. (a) Mean atmospheric river (AR) temperature by month and study region. Inset map shows the five West Coast regions of landfall analyzed in this study: Washington (WA), Oregon (OR), Northern California (N CA), Central California (C CA), and Southern California (S CA). (b) Monthly mean background temperatures for each region. (c) AR temperature from (a) minus background temperature from (b). All temperature is over the time period of 1980–2016 and vertically averaged from 1000 to 750 hPa. Outlines on triangles indicate month-regions in which the distribution of AR temperature is significantly distinct ($p < 0.05$) from that of background temperature. To assess significance at each month-region, we use the Kolmogorov-Smirnov test on the monthly mean populations of AR and background temperatures, respectively ($N = 37$ for each population by month-region).

Recent work has identified IVT as the variable most suited for AR detection (Guan & Waliser, 2015; Lavers et al., 2012). The use of IVT rather than integrated water vapor captures wind-driven moisture transport. IVT therefore better corresponds to the orographically induced precipitation characteristic of ARs (Neiman et al., 2002; Ralph et al., 2013) and is more correlated with cool-season precipitation in the western U.S. (Rutz et al., 2014).

As originally defined in MBM16 (and later modified and detailed in Ralph et al., 2018), the AR detection algorithm is based on IVT anomalies, where IVT is adjusted for its seasonal cycle at each grid box to yield a seasonally corrected IVT anomaly. A 94th percentile threshold of the IVT anomaly is then applied to distinguish AR objects. Geometric constraints are also applied. These include length and aspect ratio constraints and specific constraints designed to remove IVT objects with tropical-cyclone-like features. Therefore, note that it is possible for an area of high IVT to be omitted from the AR catalog. The AR detection process results in AR object masks projected on a latitude/longitude grid. The catalog used in this study provides time stamps of landfalling ARs detected at grid boxes along the U.S. West Coast (Figure S1).

2.4. AR Temperature Metric

We select reanalysis fields for ARs detected during the cool season (October to March). For each cool-season AR date stamp, we use daily specific humidity, zonal wind, meridional wind, and air temperature fields from each reanalysis product. We calculate IVT following Lavers et al. (2012) and others by vertically integrating water vapor transport from 1000 to 300 hPa:

$$\mathrm{IVT} = \sqrt{\left(\frac{1}{g}\int_{1000\ \mathrm{hPa}}^{300\ \mathrm{hPa}} qu\ dp\right)^2 + \left(\frac{1}{g}\int_{1000\ \mathrm{hPa}}^{300\ \mathrm{hPa}} qv\ dp\right)^2}$$

where g is acceleration due to gravity, q is specific humidity, u is the zonal component of wind, and v is the meridional component at each pressure level.

After calculating IVT for dates identified in the AR catalog, we determine AR event temperature. The purpose of our temperature metric is to capture the temperature of ARs over the landfall regions, since that is where hydroclimatic impacts occur. We thus calculate AR temperature for each region separately.

The MBM16 catalog was defined using only the MERRA-2 reanalysis. We find that IVT distributions—including absolute IVT magnitude—vary across reanalyses on AR days (supporting information Figure

S3). In particular, the distribution of NCEP-DOE IVT values is much lower than MERRA-2 and ERA-I (supporting information Figure S3). Therefore, in order to calculate AR temperature across the multiple reanalysis data sets, we first define AR presence based on the dates identified in the MBM16 catalog. After subselecting those dates in each reanalysis data set, we apply a relative IVT threshold that accounts for these IVT differences across reanalysis products by normalizing to the AR day IVT distribution in each reanalysis data set.

For each reanalysis product, we first subselect the days identified in the MBM16 catalog. Next, we select grid points on each AR day for which the absolute value of IVT exceeds that reanalysis product's 50th percentile of AR day IVT values over an East Pacific/West Coast domain (supporting information Figure S3). (The magnitude of the absolute IVT threshold is 163 kg/m/s for MERRA-2, 162 kg/m/s for ERA-I, and 139 kg/m/s for NCEP-DOE.) This threshold allows us to measure the temperature of grid points that fall in the top half of that reanalysis product's IVT distribution for the days that the MBM16 catalog determined that an AR was present. We stress that the threshold itself does not define whether IVT features are ARs—that is the role of AR catalogs. Thus, to generate the ensemble-mean AR temperature time series, AR objects must exist in the MBM16 AR catalog as originally detected on MERRA-2, but only those grid points that reach the reanalysis-specific AR intensity threshold within the landfalling region are included in the temperature calculation. This additional IVT constraint is necessary for generalizing our analysis framework across multiple reanalysis products and AR catalogs, as AR catalogs are often specific to a single reanalysis product and often only provide time stamps of AR occurrence (rather than masks of AR features detected in the particular reanalysis product).

For each region, we first remove AR days that do not contain grid boxes reaching the IVT threshold anywhere over the region. We then average AR temperatures over grid boxes reaching the IVT threshold in the horizontal dimension and from 1000 to 750 hPa in the vertical dimension. We analyze air temperature only up to 750 hPa because the majority of AR moisture is present at the lower levels of the atmosphere (Ralph et al., 2004, 2005). This process is conducted for each reanalysis product separately, resulting in three daily scale time series of AR temperature, which we subsequently average together to produce a single time series of AR temperature for each region.

Depending on geometric orientation, spatial extent, and duration, a single AR object may make landfall in more than one region, potentially at different points in its life cycle. However, due to the narrow width of ARs, some ARs only make landfall in one region, while others make landfall on different days and/or with different local temperatures. Thus, given the long and narrow spatial scales of ARs and the large geographic variations in temperature for a single landfalling AR object, we select AR events—and determine their temperatures—separately for each region. Supporting information Table S1 quantifies the number of ARs that are cross counted in each region.

2.5. AR Landfall Temperature Trend Assessment

We calculate the trend in the overall time series of cool-season mean AR temperature (October to March) for each region along the U.S. West Coast. January to March of each season are associated with the previous calendar year or current water year. We also assess AR temperature trends binned by each cool-season month. To do this, we analyze trends in the time series of monthly mean temperature for each individual month—six time series, each with 37 values—in order to equally weight each month's average temperature regardless of the number of AR occurrences in a particular month.

We calculate all trends using linear regression and assess the statistical significance of trends using an F test. We follow the Intergovernmental Panel on Climate Change (IPCC, 2014) in reporting the *change over period* (Δ) as the slope of the time series multiplied by the number of years in the time series.

2.6. Background and AR Track Temperature Trends

2.6.1. Background Temperature Trends at Landfall Destination

We assess the linear trend of monthly mean temperature from 1980 to 2016 over each of the five West Coast regions. In order to compare directly with the landfalling AR temperature trends, we average the monthly mean ERA-I, MERRA-2, and NCEP-DOE temperature values over the same portion of the lower troposphere as the AR temperature analysis (1000 to 750 hPa).

2.6.2. Coastal AR Temperature Trends Prelandfall

To assess the possible influence of trends in coastal SSTs on landfalling AR temperature trends, we calculate the trends in AR temperature over a coastal oceanic region associated with each landfall region. This analysis is conducted in the same manner as AR landfall trends (described in section 2.5), except that the regions are shifted to the west by 8° of longitude, in order to cover the coastal ocean area directly adjacent to the regions of landfall (supporting information Figure S4).

2.6.3. Along-Track AR Algorithm

We calculate the trends in AR track temperatures using individual AR tracks across the North Pacific basin. To obtain the prelandfall AR locations through time, we employ an AR tracking algorithm to detect the prelandfall locations of the ARs detected by the MBM16 algorithm in the MERRA-2 reanalysis. We employ the tracking algorithm in MERRA-2 and then characterize AR track temperature in all three reanalyses used in this study (section 2.6.4).

The tracking algorithm first searches for a detected AR within each region during the day of landfall. Given an AR detected within the landfall region, the algorithm records the feature's IVT-weighted centroid to define the AR's location in time and space, as in MBM16. At this step, the AR object is given a unique tracking label. Next, the algorithm generates a 3° × 3° tracking box around the AR feature's centroid. (We chose the 3° × 3° size of the tracking box in concordance with the expected propagation speed of an AR's centroid; abrupt changes in AR shape could generate large changes in AR centroid location between time stamps, although the actual calculated tracks shown in Figure 3 suggest that this is rare.) The algorithm then examines the previous 6-hourly time step (e.g., 12 to 6 UTC or 0 to 18 UTC on the previous day). If AR grid cells are located within the box around the centroid, then the algorithm considers this AR to be the same AR at the subsequent time step. The algorithm adds this centroid location to the track and generates a new box over the new centroid. If two AR features are located within the box during the tracking process then the algorithm retains the feature with the closest centroid. The process continues, proceeding incrementally backward in time, until there is no AR within the box. We consider this final time step as the time of AR genesis and save the AR centroid as the genesis point. We retain the entire spatiotemporal series of AR track points as a full AR track. This process generates track information for each AR, including the AR centroid's latitude and longitude for each time stamp. Backtracked AR objects that split are all considered part of the full AR track associated with the AR landfall event.

2.6.4. Along-Track AR Temperature

We calculate mean lower atmospheric temperature (1000 to 750 hPa) of each AR along the respective tracks computed in section 2.6.2. Following the use of the AR object's centroid to characterize AR track location in space and time in previous studies (MBM16; Payne & Magnusdottir, 2014), we use the centroid point to characterize AR track temperature. Therefore, for each time step in the AR track, we characterize AR track temperature using the vertical mean temperature (1000 to 750 hPa) in each of the three reanalyses at the grid point associated with the AR centroid ($N = 49{,}199$ track points for each reanalysis). We repeat this process for each reanalysis product and then average the track temperatures between reanalyses to produce the ensemble mean track temperatures.

To assess trends in monthly AR track temperatures, we first bin the AR track temperatures (at native resolution across the Pacific basin) by destination region and month of occurrence. For each month-region, we then calculate monthly mean AR track temperature across all AR track temperatures over the Pacific basin (resulting in a monthly mean time series of $N = 37$). To quantify long-term trends by month and region, we perform linear regression on the time series of monthly mean AR track temperature.

2.6.5. Trend Type Comparison

To investigate possible influences on AR landfall temperature trends (hereafter $AR_{landfall}$), we compare the magnitudes of $AR_{landfall}$ temperature trends with (1) background temperature trends at the destination region ($BK_{landfall}$), (2) temperature trends along the AR tracks (AR_{track}), and (3) AR temperature trends in coastal oceanic regions adjacent to the regions of landfall (AR_{coast}) as an indicator of the influence of coastal SSTs. For each month at each region (hereafter month-region), we calculate the trend closest to the $AR_{landfall}$ trend (in °C) by comparing the absolute values of $|BK_{landfall} - AR_{landfall}|$, $|AR_{track} - AR_{landfall}|$, and $|AR_{coast} - AR_{landfall}|$, and note the trend ($AR_{track}$, AR_{coast}, or $BK_{landfall}$) that is closest to $AR_{landfall}$ (i.e., the minimum of $|BK_{landfall} - AR_{landfall}|$, $|AR_{coast} - AR_{landfall}|$, and $|AR_{track} - AR_{landfall}|$; see supporting information Figure S5).

To evaluate if the closest trend to $AR_{landfall}$ is significantly closer than the second closest trend at a given month-region, we then compare the absolute values of the closest and second closest trend. For each month-region, we define this difference as Δ *trend proximity* (see schematic in supporting information Figure S5). Given the background climate variability, some differences between the four AR trend types are likely to arise by chance. In order to distinguish differences in the trend types from this background noise, we estimate the distribution of Δ trend proximity by sampling random $BK_{landfall}$, AR_{coast}, and AR_{track} trend proximity magnitudes ($|BK_{landfall} - AR_{landfall}|$, $|AR_{coast} - AR_{landfall}|$, and $|AR_{track} - AR_{landfall}|$) across all month-regions, taking the difference between the closest and second closest values to obtain Δ trend proximity, and repeating 100,000 times. Then, from the distribution of bootstrapped Δ trend proximity (Figure S5), we choose the value that corresponds to two standard deviations (0.56 °C) as the threshold for identifying Δ trend proximity values larger than the background noise. Thus, for a given month-region, if the difference in proximity of closest and second closest trend is larger than 0.56 °C, then the closest trend magnitude is considered *significantly closest*.

3. Results

3.1. AR Temperature Climatology

We calculate mean AR temperature (1980–2016) for each landfall region during each cool-season month (Figure 1a). Monthly mean AR temperature exhibits a consistent seasonality across the regions: the warmest ARs occur in the early months of the cool season, with ~4 °C of cooling between October and December. However, the absolute magnitude of regional mean AR temperatures varies strongly by latitude (e.g., the December mean is 3 °C in Washington and 10 °C in Southern California), with all months exhibiting a negative south-to-north temperature gradient. Differences in monthly mean temperature between adjacent regions are generally ~1–2 °C, with Washington ARs exhibiting mean temperatures that are ~7 °C cooler than Southern California ARs across the seasonal cycle.

Although background regional temperatures exhibit a similar seasonal cycle (Figure 1b), the relationship between regional mean AR temperatures and background temperatures is not consistent across the regions (Figure 1c). First, AR temperatures exhibit less regional variation than background temperatures, with inter-regional spread of ~7 °C for AR temperatures (Figure 1a) and ~9 °C for background temperatures (Figure 1b). Second, monthly mean AR temperatures are generally warmer than the background in the three northernmost regions and cooler than the background in Southern California (Figure 1c). Central California represents the approximate midpoint of this gradient, with AR temperatures and background temperatures exhibiting statistically similar values in all months except October and January. Overall, 19 of 30 month-regions contain monthly AR temperatures that are significantly different ($p < 0.05$) than the respective monthly background temperatures. The largest concentration of significant differences occurs in the northern regions from November to March.

3.2. AR Temperature Trends

In four of the five regions, we find statistically significant trends in the overall time series of cool-season AR temperature (Figures 2a–2e). The trends are positive in all regions, with magnitudes of warming between 0.69 and 1.65 °C over the 37-year study period. The magnitude and statistical significance of warming increases to the south, with the Southern and Central California regions exhibiting warming significant at $p < 0.01$, Northern California at $p = 0.03$, Oregon at $p = 0.09$, and Washington at $p = 0.15$.

Trends in the seasonal-scale AR temperature time series (Figure 2) could result from seasonal redistribution of ARs within the seasonal temperature cycle (Figure 1a), if there was a relative increase in frequency in warmer months and/or a relative decrease in frequency in cooler months. Although there has been a significant increase in March AR days in the Washington and Oregon regions (supporting information Table S2), we find no significant changes in the other 28 month-regions. Therefore, the results do not support a seasonal redistribution.

In contrast, we find positive trends in monthly scale temperature trends in most month-regions (Figures 2f–2j), with varying magnitude of trends, and significance in select months and regions. Specifically, the highest magnitudes of warming are in Southern California in January (2.19 °C), Central California in March (2.18 °C), and Northern California in March (1.91 °C). March exhibits

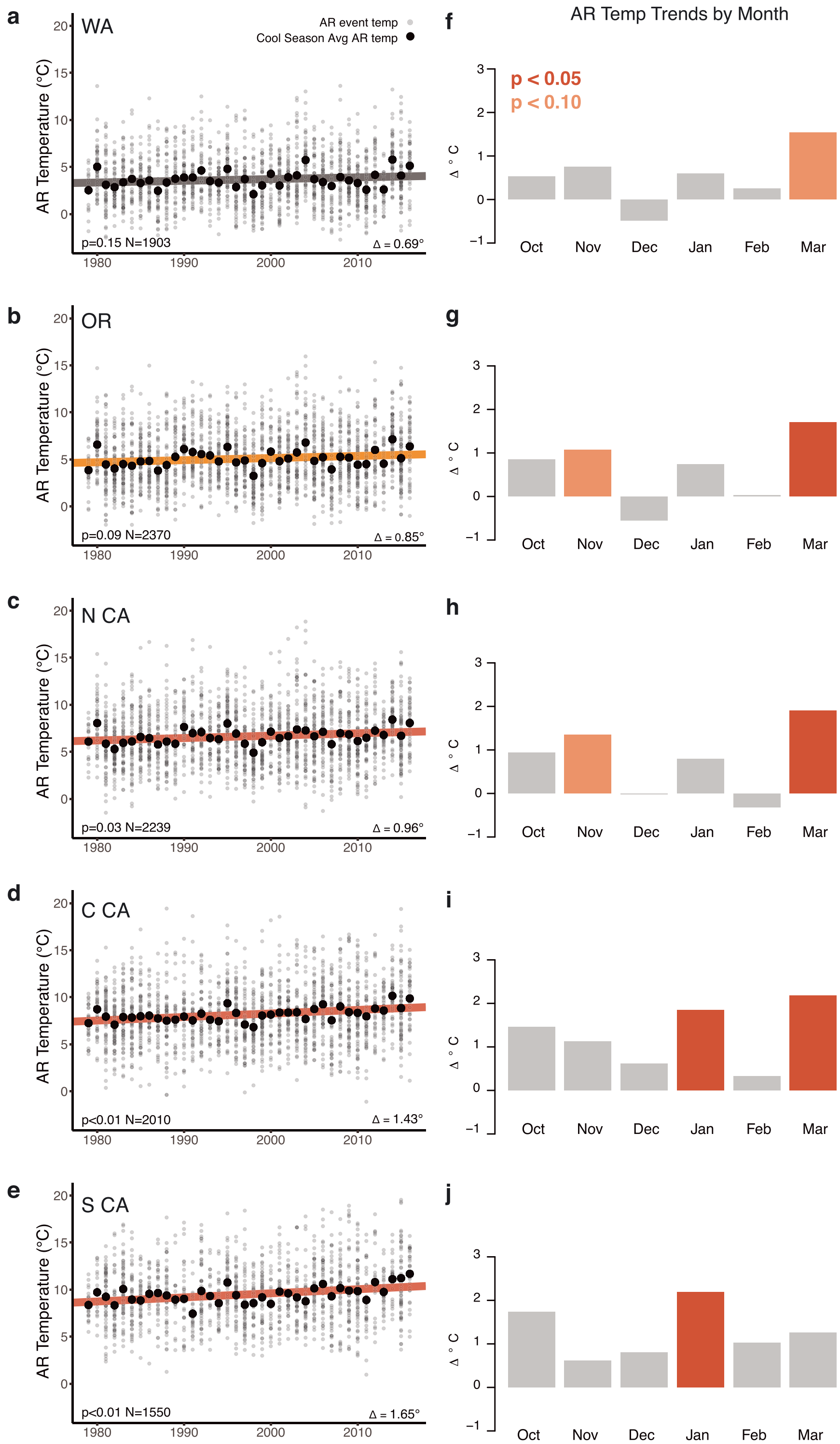

Figure 2. (a–e) Overall cool-season mean (October–March) AR temperature time series (black dots) for each region 1980–2016. All AR event temperatures are displayed in the background (gray dots). Trend is calculated on the cool-season mean time series. Thick lines show the trend in cool-season mean AR temperature, and colored trend lines denote the statistical significance of the trend (red for $p < 0.05$, orange for $p < 0.10$, and gray for $p > 0.10$). Change over time (Δ) reports the slope of the trend multiplied by the number of years (37). N is the number of total AR events for that region. All temperatures are averaged from 1000 to 750 hPa. (f–j) Change over time (Δ) of AR temperatures binned by month. Colored bars signify statistical significance (red for $p < 0.05$, orange for $p < 0.10$, and gray for $p > 0.10$).

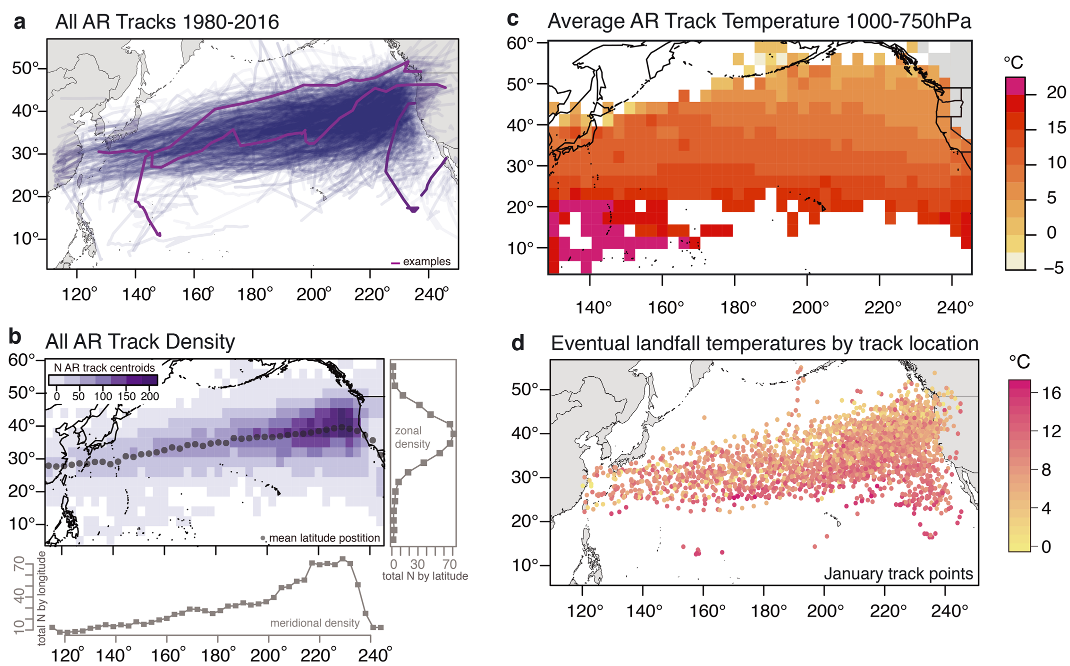

Figure 3. (a) Tracks for all West Coast landfalling ARs. Tracks are generated from AR object centroid locations from genesis to landfall every 6 hr. Highlighted tracks are selected to exemplify different track orientations: two relatively zonal tracks, one of which curves west before traveling east, and two relatively meridional, one of which originates near the coast. (b) Total track density for every track occurrence from (a), gridded onto 3° × 3° grid. Gray dots denote the weighted mean latitude position for all tracks at that particular longitude bin. Profiles on the right and the bottom denote zonal and meridional totals, respectively. (c) Overall mean cool-season AR track temperature from 1000 to 750 hPa at each 3° × 3°grid box for all AR track occurrences. Grid boxes more than 4° inland from the coast are shown in gray. (d) Track centroid locations for each AR track that occurs in January, colored by eventual temperature at landfall.

statistically significant warming trends across the West Coast (p = 0.07 in Washington, p = 0.04 in Oregon, p = 0.02 in Northern California, and p = 0.01 in Central California), with the exception of Southern California (p = 0.17). November warming is robust in Oregon and Northern California (p = 0.10 and p = 0.05, respectively), and January warming is robust in Central California and Southern California (p = 0.04 and p = 0.03, respectively). As with the warming in the overall time series (Figures 2a–2e), the smallest monthly scale warming occurs in Washington (Figure 2f). The trend results for each of the three reanalysis products are separately presented in supporting information Tables S3–S5.

We conduct a sensitivity test of the AR trends in Figure 2 by removing the years 2014 and 2015 when extremely warm coastal SSTs were present (i.e., the period during which *the Blob* of warm SSTs was present across the northeastern Pacific; Bond et al., 2015). This sensitivity test still yields statistically significant cool-season trends in Northern California, Central California, and Southern California, with significant trends in March in Northern California, March in Central California, and October in Central California (supporting information Table S6). Washington and Oregon show the greatest sensitivity to the presence of 2014 and 2015 in the analysis, as none of the AR temperature trends in those two regions are statistically significant when these years are removed (supporting information Table S6).

3.3. Comparison of AR Versus Background Temperature Trends

3.3.1. AR Tracks and Temperature

AR tracks generally follow a southwest-to-northeast trajectory over the Pacific (Figure 3a), consistent with the IVT object tracks of Sellars et al. (2017) and the path of the Pacific storm track (e.g., Lora et al., 2017). However, some ARs take a more meridional path, particularly those originating over the eastern tropical Pacific (example track highlighted in Figure 3a). Our analysis shows that ARs making landfall in the southwest U.S. often originate closer to the coast (example track highlighted in Figure 3a), consistent with the recent AR trajectory analysis of Zhang and Villarini (2018). Some AR tracks with tropical origins in the far West Pacific first travel westward—in the opposite direction of the prevailing midlatitude westerly winds—before eventually recurving toward the northeast (example track highlighted in Figure 3a). This

10.1029/2018JD029860

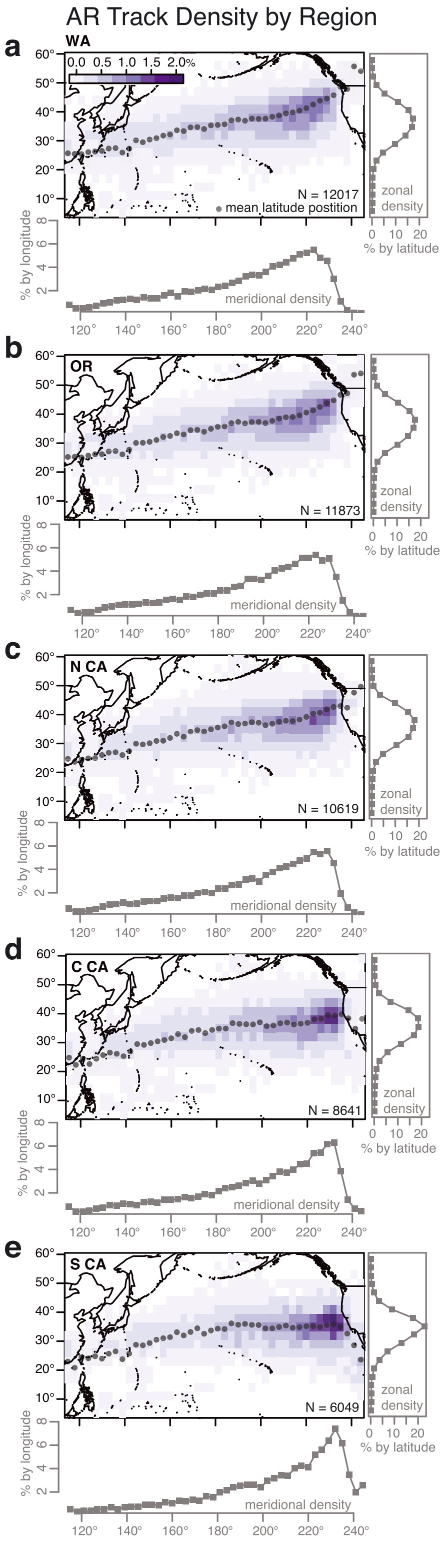

Figure 4. AR track density percentage by region of eventual landfall. Density is calculated as in Figure 3b, but with each grid box total divided by the total number of occurrences over the entire domain (denoted in the lower right corner of each panel). As in Figure 3b, gray dots denote weighted mean latitude position for all tracks at that particular longitude bin. Right/bottom profiles denote zonal/meridional density, respectively.

behavior is strongly suggestive of ARs resulting directly or indirectly from the remnants of West Pacific tropical cyclones (e.g., Cordeira et al., 2013; Hatchett, 2018).

Overall, mean AR track temperature over the North Pacific basin (Figure 3c) varies by latitude, with temperatures exceeding 20 °C in the tropics and falling below 5 °C across the North Pacific. Mean track temperature also varies by longitude, with warmest temperatures in the southwest Pacific and coolest in the northeast Pacific. The overall southwest-to-northeast gradient in track temperatures (Figure 3c) resembles the southwest-to-northeast trajectory taken by the majority of ARs (Figures 3a and 3b). In addition, the north-south temperature gradient in mean AR landfall temperature (Figure 1a) is also evident in AR track temperatures (Figure 3c).

The latitudinal dependence of AR temperature seen in the mean AR track temperature is also seen in the individual AR point temperatures, with ARs that pass over oceanic regions in the south having eventual landfall temperatures that are generally warmer (Figure 3d). However, as illustrated in Figure 3d, the eventual AR temperature at landfall can vary substantially even for tracks that pass in close proximity to each other. (Note that Figure 3d only includes AR tracks that occur in January, so the variability of track temperature is not due to the seasonal cycle.)

3.3.2. AR Track Density

The pattern of AR track density and its associated mean latitude positions (Figure 3b) tend to follow the southwest-to-northeast pattern of AR track orientation seen in Figure 3a (i.e., the positions increase in latitude as longitude increases to the west). The most prominent exceptions occur east of 220°W, where the mean latitude positions are displaced southward due to the relative abundance of subtropical and tropical AR tracks.

Figure 4 demonstrates how the spatial distributions of AR tracks vary by region of landfall, including variations in zonal and meridional density. This variation arises partly because the highest track densities are found between 220°W and 240°W—the longitudes closest to the ultimate landfall locations (Figures 3a and 3b). As a result, in the eastern Pacific, the curve of mean latitude position exhibits a southwest-northeast, or diagonal, orientation for the Washington and Oregon regions (Figures 4a and 4b) and a relatively zonal orientation for the California regions (Figures 4c–4e). However, the zonal distributions of track density exhibit far less latitudinal variation between the regions—particularly for the four northernmost regions—suggesting that West Coast ARs pass through similar regions (and therefore regions of similar temperature) prior to approaching landfall. The high density of tracks offshore of Central California and Southern California could reflect the geometry of the coastline, the relative abundance of shorter track ARs in these domains, and/or regional circulation differences that influence the trajectories of ARs as they approach the coast.

The spatial distribution of AR track density also varies through the seasonal cycle (Figure 5), which may have implications for AR track temperature and associated trends. In particular, the mean latitude positions migrate south as the season progresses. This seasonal progression is also reflected in the zonal distributions of track density. October and November exhibit the highest density of tracks in the tropical western Pacific (Figures 5a and 5b), possibly corresponding to transitioning West

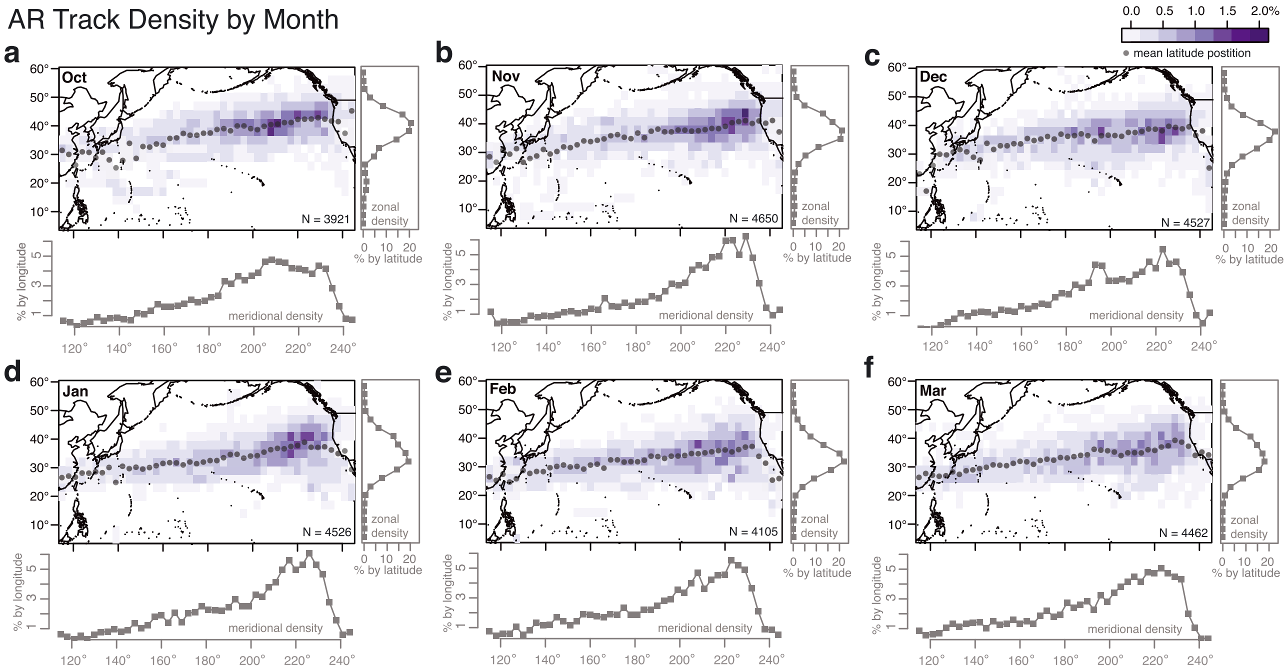

Figure 5. AR track density percentage as in Figure 4, but by month of the cool season. For each month, tracks from all landfall regions are included.

Pacific typhoons/tropical cyclones that result in warm ARs (Hatchett et al., 2018). February and March exhibit the highest density of tracks in the subtropical eastern Pacific between the Hawaiian Islands and North America (Figures 5e and 5f), coincident with the seasonal cycle of the subtropical branch of the Pacific jet, which extends farther southeastward across the basin later in the season (e.g., Neelin et al., 2013; Swain et al., 2016).

3.4. Trends in AR Landfall Temperature, AR Track Temperature, Coastal Temperature, and Regional Background Temperature

We compare AR temperature trends at landfall ($AR_{landfall}$) with along-track AR temperature trends (AR_{track}), monthly mean background temperature trends at the landfall region ($BK_{landfall}$), and AR temperature trends over the ocean adjacent to the landfall region (AR_{coast}). Figure 6 shows the magnitudes and significance levels of each trend type for each month and landfall region, along with the proximity of the AR_{track}, AR_{coast}, and $BK_{landfall}$ trend magnitudes to the $AR_{landfall}$ trend magnitude.

$BK_{landfall}$ trends are mostly positive (Figure 6). In total, of the 30 $BK_{landfall}$ trends, 5 exhibit statistically significant warming. In January, $BK_{landfall}$ trends are positive—and of higher magnitude than $AR_{landfall}$ trends—across all regions. In contrast, December $BK_{landfall}$ trends are close to zero across all regions.

AR_{coast} trends are consistently similar to $AR_{landfall}$ trends, regardless if either have exhibited significant warming, suggesting that the ocean influences air temperature trends in ARs prior to landfall. At the same time, AR_{coast} trend magnitudes are almost always less than $AR_{landfall}$ trends (in 28 of 30 instances), even if slightly, confirming that the air in ARs over the ocean has warmed less than the air in ARs over land.

AR_{track} trend magnitudes are generally smaller than $AR_{landfall}$ trend magnitudes, and there is only one instance of a statistically significant AR_{track} trend (Figure 6). The Southern California AR_{track} trends exhibit the greatest variability across the seasonal cycle. For the other four regions, there is a general decrease in AR_{track} trend magnitude as the season progresses from October to February. In March, AR_{track} trend magnitude is near zero or negative across all regions (Figure 6), despite the robust warming of $AR_{landfall}$ temperatures (Figure 2).

Using our metric of trend proximity (see section 2; Table S7), we find three instances where the $AR_{landfall}$ trend is significantly closest to the AR_{coast} trend and two instances where the $AR_{landfall}$ trend is

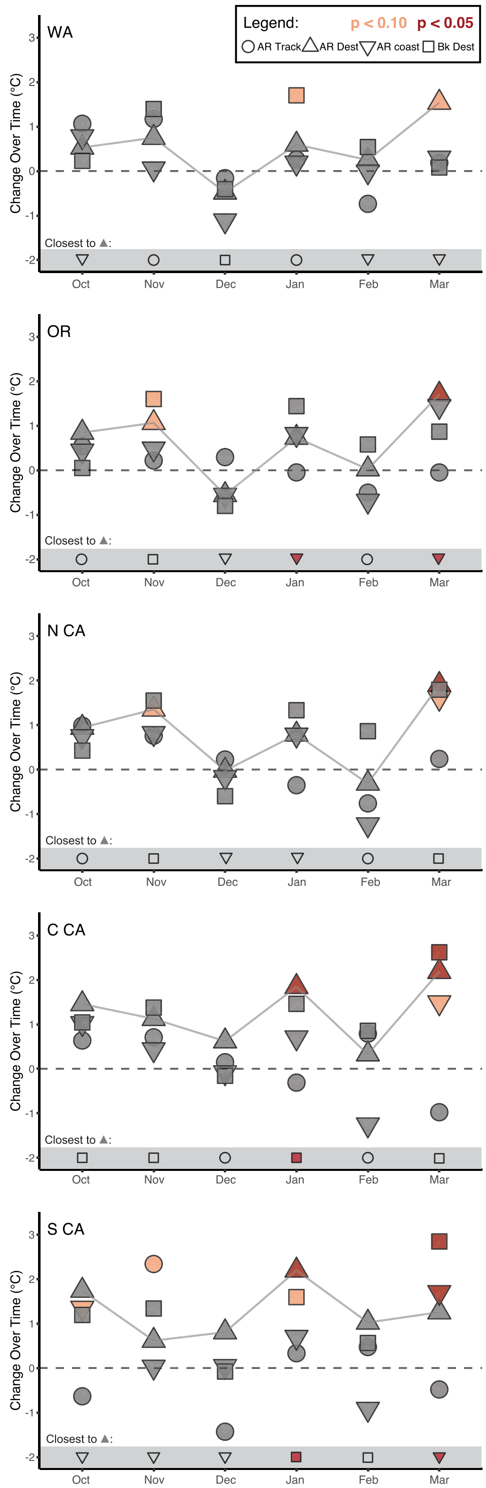

Figure 6. For each region, monthly trends in AR temperature at the landfall destination (AR$_{landfall}$), AR temperature over the AR tracks (AR$_{track}$), AR temperature over the prelandfall coastal regions (AR$_{coast}$), and background temperature at the landfall destination (BK$_{landfall}$). AR$_{landfall}$ trends are identical to those in Figures 2f–2j. Significance of trend is denoted by colored symbols (orange for $p < 0.10$ and red for $p < 0.05$). Smaller symbols in the lower gray portion for each month denote which trend (AR$_{track}$, AR$_{coast}$, or BK$_{landfall}$) is closest to AR$_{landfall}$ (see section 2).

significantly closest to the BK$_{landfall}$ trend (Figure 6). The two instances where the AR$_{landfall}$ trend is closer to the BK$_{landfall}$ trend occur in January in Central California and Southern California, and in both cases the AR$_{landfall}$ warming is of higher magnitude than the other trend types. In March, when there is strong AR$_{landfall}$ warming, AR$_{landfall}$ trend magnitudes are near AR$_{coast}$ and/or BK$_{landfall}$ trends across the regions. Also in March, the Washington AR$_{landfall}$ trend demonstrates AR$_{landfall}$ warming of higher magnitude than any of the other trend types.

Our motivation for comparing the various trends is to disentangle the causes of AR$_{landfall}$ warming. Overall, the results exhibit variation depending on region and month. The broad patterns of closest trend types suggest that AR$_{landfall}$ trends generally tend to be either dominated by strong BK$_{landfall}$ or AR$_{coast}$ warming or by a blend of AR$_{track}$, BK$_{landfall}$, and AR$_{coast}$ trends.

4. Discussion

4.1. AR Temperature Climatology

This study provides the first climatology of U.S. West Coast cool season AR temperatures. We expand upon previous analyses of AR temperature by evaluating temperatures integrated through the entire lower tropospheric column—rather than using surface air temperature, which can exhibit greater variance due to local geographic or microclimatic effects. We find that climatological AR temperatures are warmer than background temperatures in the Washington, Oregon, and Northern California regions, consistent with a previous assessment of California mean surface temperature during AR events (Dettinger, 2011). However, we find that mean AR temperatures in Central California and Southern California tend to be similar or even slightly cooler than background temperatures.

The narrower range in mean AR temperature values (~7 °C; Figure 1a) compared to background values (~9 °C; Figure 1b) suggests common source regions, pathways, moisture sources, and/or processes over the ocean that influence resultant AR temperature at landfall. Figure 3a supports this interpretation, as AR tracks for different landfall regions share some similar source regions and path trajectories, although that similarity varies by latitude. Washington and Oregon AR temperatures are consistently warmer than the background, suggesting that Washington- and Oregon-bound ARs advect warmer temperatures from the ocean and/or southern latitudes. Similarly, for most of the year, Central California and Southern California exhibit AR temperatures that are similar to or cooler than the background regional temperature, which is consistent with the tracks in Figures 3a and 4, which often originate closer to the region of landfall. Additionally, in contrast with generally cool background conditions in the northern regions, the background temperature in the southern regions tends to be warmer and therefore closer to AR temperature.

4.2. AR Temperature Trends

We find that AR temperatures at landfall have warmed across all U.S. West Coast regions during the 1980–2016 period, with statistically significant warming over all regions except Washington. The magnitude of cool-season warming is substantial, ranging from 0.69 to 1.65 °C of change over the 37-year period. At the monthly scale, the magnitude of warming in some months/regions is >2 °C (specifically Southern California in January and Central California in March), which exceeds that of late-century projections in previous work analyzing surface temperature associated with ARs (Dettinger, 2011). Depending on regional characteristics (e.g., latitude and topography), this magnitude of AR warming may have substantial implications for water resources and flood risk.

Globally, change in precipitation phase from snow to rain occurs between −2 and +4 °C over land (Dai, 2008), although the temperature range for that transition may be lower for our study regions (e.g., −2 to +2 °C in the Pacific Northwest; Nolin & Daly, 2006). Although the monthly mean temperature of West Coast landfalling ARs exhibits a range of 3 to 13 °C (Figure 1), multiple regions (Washington, Oregon, and Northern California) exhibit individual AR-mean temperatures close to 0 °C (gray dots in Figures 2a–2c), and many more events likely have local temperatures at higher elevations that are near 0 °C. The fact that AR temperatures are often close to freezing indicates that local AR precipitation is frequently near the threshold for transitioning from snow to rain, and thus may be sensitive to even slight temperature increases. It has already been observed that for all western U.S. cool-season precipitation, the fraction of precipitation falling as snow has declined due to historical warming (Knowles et al., 2006; Safeeq et al., 2016). Future analysis will focus on directly assessing the contribution of AR temperature trends to historical snow trends across the West Coast regions.

The long-term warming of landfalling ARs is not distributed evenly across the seasonal cycle. The most pronounced trends occur in March, while the least robust trends occur in December and February. Further investigation is required to understand the durability and underlying causes of this seasonal asymmetry.

The seasonality of AR warming can substantially affect the risk of associated hydrometeorological impacts by shifting the rain/snow balance, the likelihood of *rain on snow* events, and the timing and intensity of subsequent runoff. For instance, warming of January ARs (Figures 2i and 2j) could be especially relevant for snowpack accumulation—both because the climatological peak in California AR frequency occurs in January/February (Mundhenk et al., 2016) and because these months are relatively cool overall (Figure 1). In contrast, rain-on-snow hazards may be exacerbated by late-season AR warming, as these hazards tend to result from anomalously warm and moist ARs, particularly toward the end of the cool season (Guan et al., 2016). Thus, in regions with substantial late winter snowpack, the robust increase of March AR temperatures (Figure 2) could increase rain-on-snow flood risk, provided that the AR warming results in a decreased snow-to-rain ratio. Even without a specific increase of rain-on-snow hazards, the strong March AR warming is a point of concern for water resources, as April 1 is considered the canonical transition between snow accumulation and decline (e.g., Bohr & Aguado, 2001; Kapnick & Hall, 2012; Mote et al., 2018).

Interpretations and implications of our findings may be sensitive to the precise magnitudes and robustness of the AR warming trends. Therefore, we note three primary sources of uncertainty in the AR trend analysis:

Length of time series. Our analysis is limited to satellite-era ARs, meaning that we are analyzing trends across 37 years of data. The limited length of the time series may result in spurious trends due to the potential for outliers to disproportionately influence the trend quantification, particularly in months with relatively fewer ARs (supporting information Figure S2). Therefore, we advise readers to interpret the trend magnitudes and p values with caution.

Differences in reanalysis products. Differences in data assimilation and atmospheric models can create differences in historical trends in different reanalyses (e.g., Trenberth et al., 2005). In addition, an IVT anomaly object at a particular time stamp might exist in MERRA-2 but not ERA-I, or vice-versa. We thus use an IVT threshold for AR presence detection at individual grid boxes in the reanalyses as described in section 2. However, differences in the historical temperature trends in any one of the reanalysis products may have impacted our aggregated trend results. Furthermore, we note that we only used three reanalysis products. Future work could expand the analysis to include additional reanalyses, as well as GCM simulations of the historical period.

AR detection algorithm. As outlined in Shields et al. (2018), algorithms for detecting AR presence use either absolute or relative vapor transport thresholds. Further, relative thresholds of IVT have been calculated from both anomalies (e.g., MBM16; Gorodetskaya et al., 2014; Shields & Kiehl, 2016a) and percentiles (e.g., Brands et al., 2016; Guan & Waliser, 2015; Lavers et al., 2012). The AR catalog based on the MBM16

10.1029/2018JD029860

algorithm defines ARs as anomalous IVT relative to the time of year and location, which is appropriate for the spatial scope of our analysis, as AR frequency along the West Coast is seasonally and latitudinally variable (Mundhenk et al., 2016). However, testing the robustness of our results to the AR detection algorithm is an important priority for future research.

4.3. Sources of AR Temperature Trends

We have quantified spatial distributions of AR tracks and AR temperatures across the North Pacific basin. These temperature and track density results demonstrate spatial variation in mean AR track temperature across the North Pacific, and spatial and seasonal variation in the locations of tracks across regions of landfall. These variations highlight that AR temperature trends could be influenced by a number of factors relating to the AR paths and/or thermodynamic environments, motivating further understanding of AR temperature evolution.

The proximity of AR_{coast} to $AR_{landfall}$ trend magnitudes suggests that the anomalously warm region of SSTs known as the Blob (Bond et al., 2015) may have played a role in the warming of $AR_{landfall}$ trends (Figure 2), as the Blob was centralized off the PNW coast in the Gulf of Alaska (Bond et al., 2015; Hu et al., 2017). This apparent sensitivity to near-coastal SSTs in the Pacific Northwest is noteworthy given recent research suggesting that climate change has substantially increased the likelihood of such extremely warm regional SSTs (Funk et al. 2014; Frölicher et al., 2018) and that marine heat waves of similar or greater magnitude will likely occur with greater frequency in the future (Di Lorenzo & Mantua, 2016). The trend comparison in Figure 6 broadly suggests that near-coastal environmental factors—including coastal SSTs and background temperatures—have more influence on $AR_{landfall}$ temperatures than do AR_{track} temperatures.

Our trend comparison suggests that neither $BK_{landfall}$, AR_{track}, nor AR_{coast} trends can solely account for all $AR_{landfall}$ trends. This ambiguity is important for future projections of AR temperature, as a null hypothesis could be to project AR landfall trends as scaling with the background regional temperature trends. However, our results suggest greater complexity that varies by region and season. Most of the monthly scale $AR_{landfall}$ trends fall between the respective $BK_{landfall}$ trend and the respective AR_{coast} or AR_{track} trend. The intermediate trend magnitudes suggest a combination of strong local warming near the coast or over land, and modest remote warming over ocean.

These results suggest a need for a more nuanced understanding of AR temperature evolution from genesis to landfall. Further research is needed that investigates the extent to which AR landfall temperatures are influenced by prelandfall characteristics of the AR and background characteristics of the landfall environment. One relevant aspect of ARs for understanding their temperature evolution is that they source moisture both locally and remotely. The majority of winter (DJF) moisture comes from the Northeast Pacific (Nusbaumer & Noone, 2018), yet a number of case studies have demonstrated examples of both large-scale advection and local moisture convergence as the dominant mechanism (e.g., Dacre et al., 2015; Sodemann & Stohl, 2013). Our results (Figure 6) likewise suggest that AR temperature evolution varies across the AR's lifespan, depending on the season and region of eventual landfall. Therefore, we emphasize that there may be a certain subset of ARs that are subject to different thermodynamic influences—especially those that are characterized by a strong tropical/subtropical advective component (e.g., Bao et al., 2006). Furthermore, there may be important three-dimensional thermodynamic processes (e.g., related to vertical temperature structure) that influence the freezing altitude and related downstream impacts. In order to project AR temperature changes and their associated impacts in the future climate, it will be important to use tools that can resolve AR processes at a sufficiently high spatial and temporal scale (e.g., Leung & Qian, 2009; Swain et al., 2015), particularly if future ARs exhibit different dynamic and thermodynamic characteristics than historical ARs.

5. Conclusions

We report substantial warming in landfalling U.S. West Coast atmospheric rivers from 1980 to 2016. Our findings have implications for future trends in AR temperatures, both on the U.S. West Coast and more broadly for other regions of AR landfall. The magnitudes of monthly scale warming (>2 °C of warming in some months/regions), as well as the seasonal asymmetry of these trends, carry important implications for flood risk and water storage—which are both sensitive to the temperature threshold for the snow-to-rain transition. In some regions and months, observed warming of ARs identified in this study exceeds climate model projections for late-century warming of AR surface temperatures documented in previous work. Our study also identifies variable influence of trends in along-track temperatures, coastal SSTs, and background regional temperatures on landfalling AR temperature trends. We find that near-coastal environmental factors (coastal SSTs and background temperatures) have scaled most closely with landfalling AR trends. Given the region's reliance on ARs for water supply and vulnerability to AR-related hazards, it will be important to further understand the causes of AR warming trends, their regional and seasonal complexities, and whether such trends are likely to persist in the future.

Acknowledgments
We thank three anonymous reviewers for their insightful and constructive comments. This work was supported in part by National Science Foundation Grant DGE-114747 and the Stanford VPGE EDGE and DARE Fellowships to K. R. G. and support from the National Science Foundation, Department of Energy and Stanford University to N. S. D. D. L. S. was supported by a joint collaboration between the Institute of the Environment and Sustainability at the University of California, Los Angeles; the Center for Climate and Weather Extremes at the National Center for Atmospheric Research; and the Nature Conservancy of California. K. M. N. was funded by a subgrant from CW3E of Scripps Institution of Oceanography under the FIRO project. E.A.B.'s contribution was performed as part of the NOAA MAPP S2S Prediction Task Force and supported by NOAA Grant NA16OAR4310064. The ERA-Interim reanalysis is available at the ECMWF website: http://apps.ecmwf.int/datasets/data/interim-full-daily/. The MERRA-2 reanalysis was downloaded at https://esgf.nccs.nasa.gov/search/create-ip/. The NCEP-DOE reanalysis is available at https://rda.ucar.edu/datasets/ds091.0. The AR detection algorithm as originally written in Mundhenk et al. (2016) is available online at http://hdl.handle.net/10217/170619.

References

Bao, J.-W., Michelson, S. a., Neiman, P. J., Ralph, F. M., & Wilczak, J. M. (2006). Interpretation of enhanced integrated water vapor bands associated with extratropical cyclones: Their formation and connection to tropical moisture. *Monthly Weather Review*, *134*(4), 1063–1080. https://doi.org/10.1175/MWR3123.1

Bohr, G. S., & Aguado, E. (2001). Use of April 1 SWE measurements as estimates of peak seasonal snowpack and total cold-season precipitation. *Water Resources Research*, *37*(1), 51–60. https://doi.org/10.1029/2000WR900256

Bond, N. A., Cronin, M. F., Freeland, H., & Mantua, N. (2015). Causes and impacts of the 2014 warm anomaly in the NE Pacific. *Geophysical Research Letters*, *42*, 3414–3420. https://doi.org/10.1002/2015GL063306

Brands, S., Gutiérrez, J. M., & San-Martín, D. (2016). Twentieth-century atmospheric river activity along the west coasts of Europe and North America: Algorithm formulation, reanalysis uncertainty and links to atmospheric circulation patterns. *Climate Dynamics.*, *48*(9-10), 2771–2795. https://doi.org/10.1007/s00382-016-3095-6

Cayan, D. R., Dettinger, M. D., Kammerdiener, S. A., Caprio, J. M., Peterson, D. H., & Cayan, D. R. (2001). Changes in the onset of spring in the Western United States. *Bulletin of the American Meteorological Society*, *82*(3), 399–415. https://doi.org/10.1175/1520-0477(2001)082<0399:CITOOS>2.3.CO;2

Cordeira, J. M., Ralph, F. M., & Moore, B. J. (2013). The development and evolution of two atmospheric rivers in proximity to western North Pacific tropical cyclones in October 2010. *Monthly Weather Review*, *141*(12), 4234–4255. https://doi.org/10.1175/MWR-D-13-00019.1

Dacre, H. F., Clark, P. A., Martinez-Alvarado, O., Stringer, M. A., & Lavers, D. A. (2015). How do atmospheric rivers form? *Bulletin of the American Meteorological Society*, *96*(8), 1243–1255. https://doi.org/10.1175/BAMS-D-14-00031.1

Dai, A. (2008). Temperature and pressure dependence of the rain-snow phase transition over land and ocean. *Geophysical Research Letters*, *35*, L12802. https://doi.org/10.1029/2008GL033295

Das, T., Dettinger, M. D., Cayan, D. R., & Hidalgo, H. G. (2011). Potential increase in floods in California's Sierra Nevada under future climate projections. *Climatic Change*, *109*(S1), 71–94. https://doi.org/10.1007/s10584-011-0298-z

Dee, D. P. (2011). The ERA-Interim reanalysis: Configuration and performance of the data assimilation system. *Quarterly Journal of the Royal Meteorological Society*, *137*(656), 553–597. https://doi.org/10.1002/qj.828

Dettinger, M. (2011). Climate change, atmospheric rivers, and floods in California—A multimodel analysis of storm frequency and magnitude changes. 1. *Journal of the American Water Resources Association*, *47*(3), 514–523. https://doi.org/10.1111/j.1752-1688.2011.00546.x

Di Lorenzo, E., & Mantua, N. (2016). Multi-year persistence of the 2014/15 North Pacific marine heatwave. *Nature Climate Change*, *6*(11), 1042–1047. https://doi.org/10.1038/nclimate3082

Diffenbaugh, N. S., Swain, D. L., & Touma, D. (2015). Anthropogenic warming has increased drought risk in California. *Proceedings of the National Academy of Sciences*, *112*(13), 3931–3936. https://doi.org/10.1073/PNAS.1422385112

Espinoza, V., Waliser, D. E., Guan, B., Lavers, D. A., & Ralph, F. M. (2018). Global analysis of climate change projection effects on atmospheric rivers. *Geophysical Research Letters*, *45*, 4299–4308. https://doi.org/10.1029/2017GL076968

Frölicher, T. L., Fischer, E. M., & Gruber, N. (2018). Marine heatwaves under global warming. *Nature*, *560*(7718), 360–364. https://doi.org/10.1038/s41586-018-0383-9

Gao, Y., Lu, J., Leung, L. R., Yang, Q., Hagos, S., & Qian, Y. (2015). Dynamical and thermodynamical modulations on future changes of landfalling atmospheric rivers over western North America. *Geophysical Research Letters*, *42*, 7179–7186. https://doi.org/10.1002/2015GL065435.Received

Gelaro, R., McCarty, W., Suárez, M. J., Todling, R., Molod, A., Takacs, L., et al. (2017). The Modern-Era Retrospective Analysis for Research and Applications, Version 2 (MERRA-2). *Journal of Climate*, *30*(14), 5419–5454. https://doi.org/10.1175/JCLI-D-16-0758.1

Gershunov, A., Shulgina, T., Ralph, F. M., Lavers, D. A., & Rutz, J. J. (2017). Assessing the climate-scale variability of atmospheric rivers affecting western North America. *Geophysical Research Letters*, *44*, 7900–7908. https://doi.org/10.1002/2017GL074175

Gorodetskaya, I. V., Tsukernik, M., Claes, K., Ralph, M. F., Neff, W. D., & Van Lipzig, N. P. M. (2014). The role of atmospheric rivers in anomalous snow accumulation in East Antarctica. *Geophysical Research Letters*, *41*, 6199–6206. https://doi.org/10.1002/2014GL060881

Guan, B., Molotch, N. P., Waliser, D. E., Fetzer, E. J., & Neiman, P. J. (2010). Extreme snowfall events linked to atmospheric rivers and surface air temperature via satellite measurements. *Geophysical Research Letters*, *37*, L20401. https://doi.org/10.1029/2010GL044696

Guan, B., & Waliser, D. E. (2015). Detection of atmospheric rivers: Evaluation and application of an algorithm for global studies. *Journal of Geophysical Research: Atmospheres*, *120*, 12,514–12,535. https://doi.org/10.1002/2015JD024257

Guan, B., Waliser, D. E., Ralph, F. M., Fetzer, E. J., & Neiman, P. J. (2016). Hydrometeorological characteristics of rain-on-snow events associated with atmospheric rivers. *Geophysical Research Letters*, *43*, 2964–2973. https://doi.org/10.1002/2016GL067978

Hagos, S. M., Leung, L. R., Yoon, J.-H., Lu, J., & Gao, Y. (2016). A projection of changes in landfalling atmospheric river frequency and extreme precipitation over western North America from the Large Ensemble CESM simulations. *Geophysical Research Letters*, *43*, 1357–1363. https://doi.org/10.1002/2015GL067392

Hatchett, B. (2018). Snow level characteristics and impacts of a spring typhoon-originating atmospheric river in the Sierra Nevada, USA. *Atmosphere*, *9*(6), 233. https://doi.org/10.3390/atmos9060233

Hatchett, B., Daudert, B., Garner, C., Oakley, N., Putnam, A., & White, A. (2017). Winter snow level rise in the Northern Sierra Nevada from 2008 to 2017. *Water*, *9*(11), 899. https://doi.org/10.3390/w9110899

Hu, Z.-Z., Kumar, A., Jha, B., Zhu, J., & Huang, B. (2017). Persistence and predictions of the remarkable warm anomaly in the northeastern Pacific Ocean during 2014–16. *Journal of Climate*, *30*(2), 689–702. https://doi.org/10.1175/JCLI-D-16-0348.1

Huang, X., Hall, A. D., & Berg, N. (2018). Anthropogenic warming impacts on today's Sierra Nevada snowpack and flood risk. *Geophysical Research Letters*, *45*, 6215–6222. https://doi.org/10.1029/2018GL077432

IPCC (2014). Summary for policymakers. Climate change 2014: Impacts, adaptation and vulnerability—Contributions of the Working Group II to the Fifth Assessment Report. https://doi.org/10.1016/j.renene.2009.11.012

Jackson, D. L., Hughes, M., & Wick, G. A. (2016). Evaluation of landfalling atmospheric rivers along the U.S. West Coast in reanalysis data sets. *Journal of Geophysical Research: Atmospheres*, *121*, 2705–2718. https://doi.org/10.1002/2015JD024412

Kanamitsu, M., Ebisuzaki, W., Woollen, J., Yang, S.-K., Hnilo, J. J., Fiorino, M., & Potter, G. L. (2002). NCEP–DOE AMIP-II Reanalysis (R-2). *Bulletin of the American Meteorological Society*, *83*(11), 1631–1644. https://doi.org/10.1175/BAMS-83-11-1631

Kapnick, S., & Hall, A. (2012). Causes of recent changes in western North American snowpack. *Climate Dynamics*, *38*(9–10), 1885–1899. https://doi.org/10.1007/s00382-011-1089-y

Knowles, N., Dettinger, M. D., Cayan, D. R., Knowles, N., Dettinger, M. D., & Cayan, D. R. (2006). Trends in snowfall versus rainfall in the Western United States. *Journal of Climate*, *19*(18), 4545–4559. https://doi.org/10.1175/JCLI3850.1

Lavers, D. A., Villarini, G., Allan, R. P., Wood, E. F., & Wade, A. J. (2012). The detection of atmospheric rivers in atmospheric reanalyses and their links to British winter floods and the large-scale climatic circulation. *Journal of Geophysical Research*, *117*, D20106. https://doi.org/10.1029/2012JD018027

Leung, L. R., & Qian, Y. (2009). Atmospheric rivers induced heavy precipitation and flooding in the western U.S. simulated by the WRF regional climate model. *Geophysical Research Letters*, *36*, L03820. https://doi.org/10.1029/2008GL036445

Lora, J. M., Mitchell, J. L., Risi, C., & Tripati, A. E. (2017). North Pacific atmospheric rivers and their influence on western North America at the Last Glacial Maximum. *Geophysical Research Letters*, *44*, 1051–1059. https://doi.org/10.1002/2016GL071541

Mote, P. W., Li, S., Lettenmaier, D. P., Xiao, M., & Engel, R. (2018). Dramatic declines in snowpack in the western US. *Npj Climate and Atmospheric Science*, *1*(1), 2. https://doi.org/10.1038/s41612-018-0012-1

Mundhenk, B. D., Barnes, E. A., Maloney, E. D., Mundhenk, B. D., Barnes, E. A., & Maloney, E. D. (2016). All-season climatology and variability of atmospheric river frequencies over the North Pacific. *Journal of Climate*, *29*(13), 4885–4903. https://doi.org/10.1175/JCLI-D-15-0655.1

Neelin, J. D., Langenbrunner, B., Meyerson, J. E., Hall, A., & Berg, N. (2013). California winter precipitation change under global warming in the Coupled Model Intercomparison Project Phase 5 ensemble. *Journal of Climate*, *26*(17), 6238–6256. https://doi.org/10.1175/JCLI-D-12-00514.1

Neiman, P. J., Ralph, F. M., White, A. B., Kingsmill, D. E., & Persson, P. O. G. (2002). The statistical relationship between upslope flow and rainfall in California's coastal mountains: Observations during CALJET. *Monthly Weather Review*, *130*(6), 1468–1492. https://doi.org/10.1175/1520-0493(2002)130<1468:TSRBUF>2.0.CO;2

Neiman, P. J., Schick, L. J., Ralph, F. M., Hughes, M., & Wick, G. A. (2011). Flooding in Western Washington: The connection to atmospheric rivers*. *Journal of Hydrometeorology*, *12*(6), 1337–1358. https://doi.org/10.1175/2011JHM1358.1

Nolin, A. W., & Daly, C. (2006). Mapping "at risk" snow in the Pacific Northwest. *Journal of Hydrometeorology*, *7*(5), 1164–1171. https://doi.org/10.1175/JHM543.1

Nusbaumer, J., & Noone, D. (2018). Numerical evaluation of the modern and future origins of atmospheric river moisture over the West Coast of the United States. *Journal of Geophysical Research: Atmospheres*, *123*, 6423–6442. https://doi.org/10.1029/2017JD028081

Oakley, N. S., Lancaster, J. T., Hatchett, B. J., Stock, J., Ralph, F. M., Roj, S., & Lukashov, S. (2018). A 22-Year Climatology of cool season hourly precipitation thresholds conducive to shallow landslides in California. *Earth Interactions*, *22*(14), 1–35. https://doi.org/10.1175/EI-D-17-0029.1

Payne, A. E., & Magnusdottir, G. (2014). Dynamics of landfalling atmospheric rivers over the North Pacific in 30 years of MERRA Reanalysis. *Journal of Climate*, *27*(18), 7133–7150. https://doi.org/10.1175/JCLI-D-14-00034.1

Payne, A. E., & Magnusdottir, G. (2015). An evaluation of atmospheric rivers over the North Pacific in CMIP5 and their response to warming under RCP 8.5. *Journal of Geophysical Research: Atmospheres*, *120*, 11,173–11,190. https://doi.org/10.1002/2015JD023586

Ralph, F. M., Coleman, T., Neiman, P. J., Zamora, R. J., & Dettinger, M. D. (2013). Observed impacts of duration and seasonality of atmospheric-river landfalls on soil moisture and runoff in coastal Northern California. *Journal of Hydrometeorology*, *14*(2), 443–459. https://doi.org/10.1175/JHM-D-12-076.1

Ralph, F. M., Neiman, P. J., Kiladis, G. N., Weickmann, K., & Reynolds, D. W. (2011). A multiscale observational case study of a Pacific atmospheric river exhibiting tropical–extratropical connections and a mesoscale frontal wave. *Monthly Weather Review*, *139*(4), 1169–1189. https://doi.org/10.1175/2010MWR3596.1

Ralph, F. M., Neiman, P. J., Rotunno, R., Ralph, F. M., Neiman, P. J., & Rotunno, R. (2005). Dropsonde observations in low-level jets over the northeastern Pacific Ocean from CALJET-1998 and PACJET-2001: Mean vertical-profile and atmospheric-river characteristics. *Monthly Weather Review*, *133*(4), 889–910. https://doi.org/10.1175/MWR2896.1

Ralph, F. M., Neiman, P. J., Wick, G. A., Gutman, S. I., Dettinger, M. D., Cayan, D. R., & White, A. B. (2006). Flooding on California's Russian River: Role of atmospheric rivers. *Geophysical Research Letters*, *33*, L13801. https://doi.org/10.1029/2006GL026689

Ralph, F. M., Neiman, P. J., Wick, G. A., Ralph, F. M., Neiman, P. J., & Wick, G. A. (2004). Satellite and CALJET Aircraft observations of atmospheric rivers over the eastern North Pacific Ocean during the winter of 1997/98. *Monthly Weather Review*, *132*(7), 1721–1745. https://doi.org/10.1175/1520-0493(2004)132<1721:SACAOO>2.0.CO;2

Ralph, F. M., Wilson, A. M., Shulgina, T., Kawzenuk, B., Sellars, S., Rutz, J. J., et al. (2018). ARTMIP-early start comparison of atmospheric river detection tools: How many atmospheric rivers hit northern California's Russian River watershed? *Climate Dynamics*, *52*(7-8), 4973–4994. https://doi.org/10.1007/s00382-018-4427-5

Ramos, A. M., Tomé, R., Trigo, R. M., Liberato, M. L. R., & Pinto, J. G. (2016). Projected changes in atmospheric rivers affecting Europe in CMIP5 models. *Geophysical Research Letters.*, *43*, 9315–9323. https://doi.org/10.1002/2016GL070634

Rienecker, M. M., Suarez, M. J., Gelaro, R., Todling, R., Bacmeister, J., Liu, E., et al. (2011). MERRA: NASA's Modern-Era Retrospective Analysis for Research and Applications. *Journal of Climate*, *24*(14), 3624–3648. https://doi.org/10.1175/JCLI-D-11-00015.1

Rutz, J. J., Steenburgh, W. J., & Ralph, F. M. (2014). Climatological characteristics of atmospheric rivers and their inland penetration over the western United States. *Monthly Weather Review*, *142*(2), 905–921. https://doi.org/10.1175/MWR-D-13-00168.1

Safeeq, M., Shukla, S., Arismendi, I., Grant, G. E., Lewis, S. L., & Nolin, A. (2016). Influence of winter season climate variability on snow–precipitation ratio in the western United States. *International Journal of Climatology.*, *36*(9), 3175–3190. https://doi.org/10.1002/joc.4545

Saha, S., Moorthi, S., Pan, H.-L., Wu, X., Wang, J., Nadiga, S., et al. (2010). The NCEP Climate Forecast System Reanalysis. *Bulletin of the American Meteorological Society*, *91*(8), 1015–1058. https://doi.org/10.1175/2010BAMS3001.1

10.1029/2018JD029860

Sellars, S. L., Kawzenuk, B., Nguyen, P., Ralph, F. M., & Sorooshian, S. (2017). Genesis, pathways, and terminations of intense global water vapor transport in association with large-scale climate patterns. *Geophysical Research Letters.*, *44*(24), 12,465–12,475. https://doi.org/10.1002/2017GL075495

Shields, C. A., & Kiehl, J. T. (2016a). Atmospheric river landfall-latitude changes in future climate simulations. *Geophysical Research Letters.*, *43*, 8775–8782. https://doi.org/10.1002/2016GL070470

Shields, C. A., & Kiehl, J. T. (2016b). Simulating the Pineapple Express in the Half Degree Community Climate System Model, CCSM4. *Geophysical Research Letters.*, *43*, 7767–7773. https://doi.org/10.1002/2016GL069476

Shields, C. A., Rutz, J. J., Leung, L.-Y., Ralph, F. M., Wehner, M., Kawzenuk, B., et al. (2018). Atmospheric River Tracking Method Intercomparison Project (ARTMIP): Project goals and experimental design. *Geoscientific Model Development*, *11*(6), 2455–2474. https://doi.org/10.5194/gmd-11-2455-2018

Sodemann, H., & Stohl, A. (2013). Moisture origin and meridional transport in atmospheric rivers and their association with multiple cyclones*. *Monthly Weather Review*, *141*(8), 2850–2868. https://doi.org/10.1175/MWR-D-12-00256.1

Swain, D. L., Horton, D. E., Singh, D., & Diffenbaugh, N. S. (2016). Trends in atmospheric patterns conducive to seasonal precipitation and temperature extremes in California. *Science Advances*, *2*(4). https://doi.org/10.1126/sciadv.1501344

Swain, D. L., Lebassi-Habtezion, B., & Diffenbaugh, N. S. (2015). Evaluation of nonhydrostatic simulations of Northeast Pacific atmospheric rivers and comparison to in situ observations. *Monthly Weather Review*, *143*(9), 3556–3569. https://doi.org/10.1175/MWR-D-15-0079.1

Trenberth, K. E., Fasullo, J., & Smith, L. (2005). Trends and variability in column-integrated atmospheric water vapor. *Climate Dynamics*, *24*(7-8), 741–758. https://doi.org/10.1007/s00382-005-0017-4

Waliser, D., & Guan, B. (2017). Extreme winds and precipitation during landfall of atmospheric rivers. *Nature Geoscience*, *10*(3), 179–183. https://doi.org/10.1038/ngeo2894

Warner, M. D., Mass, C. F., Salathé, E. P., Warner, M. D., & Mass, C. F. (2015). Changes in winter atmospheric rivers along the North American West Coast in CMIP5 climate models. *Journal of Hydrometeorology*, *16*(1), 118–128. https://doi.org/10.1175/JHM-D-14-0080.1

Zhang, W., & Villarini, G. (2018). Uncovering the role of the East Asian jet stream and heterogeneities in atmospheric rivers affecting the western United States. *Proceedings of the National Academy of Sciences of the United States of America*, *115*(5), 891–896. https://doi.org/10.1073/pnas.1717883115

Zhu, Y., & Newell, R. E. (1998). A proposed algorithm for moisture fluxes from atmospheric rivers. *Monthly Weather Review*, *126*(3), 725–735. https://doi.org/10.1175/1520-0493(1998)126<0725:APAFMF>2.0.CO;2